

Nanoscale

Accepted Manuscript



This is an *Accepted Manuscript*, which has been through the Royal Society of Chemistry peer review process and has been accepted for publication.

Accepted Manuscripts are published online shortly after acceptance, before technical editing, formatting and proof reading. Using this free service, authors can make their results available to the community, in citable form, before we publish the edited article. We will replace this *Accepted Manuscript* with the edited and formatted *Advance Article* as soon as it is available.

You can find more information about *Accepted Manuscripts* in the [Information for Authors](#).

Please note that technical editing may introduce minor changes to the text and/or graphics, which may alter content. The journal's standard [Terms & Conditions](#) and the [Ethical guidelines](#) still apply. In no event shall the Royal Society of Chemistry be held responsible for any errors or omissions in this *Accepted Manuscript* or any consequences arising from the use of any information it contains.

Cite this: DOI: 10.1039/c0xx00000x

www.rsc.org/xxxxxx

ARTICLE TYPE

Facile synthesis of a mesoporous Co_3O_4 network for Li-storage via thermal decomposition of an amorphous metal-complex

Wei Wen,^a Jin-Ming Wu^{*a} and Min-Hua Cao^b

Received (in XXX, XXX) Xth XXXXXXXXX 20XX, Accepted Xth XXXXXXXXX 20XX

DOI: 10.1039/b000000x

A facile strategy is developed to mass fabrications of porous Co_3O_4 network via the thermal decomposition of an amorphous cobalt-based complex. At a low mass loading, the achieved porous Co_3O_4 networks exhibit excellent performance for lithium storage, which has a high capacity of 587 mAh g^{-1} after 500 cycles at a current density of 1000 mA g^{-1} .

Lithium-ion battery (LIB) is a promising power source for portable electronics and electric vehicles because of its high energy density when compared with other energy-storage devices.¹⁻⁴ The next generation of LIBs aims at combined characteristics of high energy density, high power density, long lifetime, and low cost, especially those for electric vehicles. Since the first report by Tarascon et al.,⁵ transition metal oxides have been considered as potential anode materials for LIBs because of their much higher capacity when compared with commercial graphite (with a theoretical value of 370 mAh g^{-1}). Among them, Co_3O_4 has stimulated tremendous research interests because of its high capacity of 890 mAh g^{-1} ,⁶ however, it suffers from common drawbacks of conversion-reaction-based metal oxide anodes, that is, poor cycling stability and rate performance, due to the poor conductivity and large specific volume change during battery cycling, which leads to pulverization and detachment of active materials from the conductive substrate. To overcome these problems, Co_3O_4 in various nanostructures, such as nanoparticles,⁷ nanocubes,⁸ nanotubes,⁹ nanowires,^{10,11} nanobelts,¹² nanosheets,^{13,14} star-like structures,¹⁵ and hollow structures,^{16,17} has been fabricated and studied extensively. As an effective strategy, cobalt oxides were also composited with carbon materials to construct hybrid electrodes;¹⁸⁻²² but the presence of the low-capacity carbon suppresses the battery capacity/weight ratio and makes the synthesis process more complex. Excellent electrochemical properties have been recorded for anode materials in the form of thin films because of the much improved conductivity,²³⁻²⁶ however, their loading of active materials is too low.²⁷ Increasing the thickness of thin film anodes always sharply deteriorates the electrochemical performance.²⁶

A porous structure achieves more efficient ingress and infiltration of the electrolyte and partially accommodates the large volume change.²⁸ However, most approaches for porous transition metal oxides are template-assisted by using soft

templates or hard templates, which need troublesome multi-step procedures. Recently, a bacterial template, which is inexpensive and easy to handle, was developed to synthesize porous Co_3O_4 .²⁹ As for template-free techniques, decomposition of pre-synthesized precursors is effective to achieve porous Co_3O_4 . For example, mesoporous Co_3O_4 nanosheets were fabricated by thermal transformation of $\text{Co}(\text{OH})_2$ prepared by electrodeposition.³⁰ Mesoporous Co_3O_4 nanowires were also obtained via thermal decomposition of $\text{Co}(\text{CO}_3)_{0.5}(\text{OH})\cdot 0.11\text{H}_2\text{O}$, which is synthesized by a hydrothermal route.³¹ Recently, metal-organic frameworks (MOFs) have been recognized as promising precursors to prepare mesoporous metal oxides.³²⁻³⁶ Meng et al. prepared a cobalt-based MOF, which decomposed to porous Co_3O_4 particles via a two-step calcination treatment (in Ar gas and air).³⁴ Unfortunately, the synthesis of MOFs is relatively complex and costly.

With continuous efforts, the capacity of Co_3O_4 has been improved steadily in recent years; yet the lifetime is not satisfying.⁹⁻²¹ It thus remains an urgent task yet a challenge to further improve the rate capability and cycling stability of Co_3O_4 , especially for those fabricated by a simple and cost-effective synthesis technique.

Herein, we develop a facile strategy to mass fabrications of porous Co_3O_4 network via the thermal decomposition of an amorphous cobalt-based complex. The cobalt-based complex is prepared by a simple and rapid pyrolysis of cobalt nitrate and glycine. The achieved porous Co_3O_4 networks exhibit excellent performance for lithium storage because of the porous structure and fine nanoparticle blocks. At a low mass loading, the porous Co_3O_4 network exhibits a high capacity of 587 mAh g^{-1} after 500 cycles at a high current density of 1000 mA g^{-1} .

In preparation, 1.250 g $\text{Co}(\text{NO}_3)_2\cdot 6\text{H}_2\text{O}$ and 1.750 g glycine ($\text{C}_2\text{H}_5\text{NO}_2$) were dissolved in 10 mL deionized water in a crucible to form a pink solution, which was then transferred to a preheated furnace maintained at 400 °C for ca. 16 minutes to finish the decomposition reaction, resulting in a black precursor. The as-synthesized precursor was then heated in air at 355 °C for 1 h at a heating rate of 5 °C min^{-1} to achieve finally the porous Co_3O_4 network.

Fig. 1 illustrates schematically the synthesis procedure for mass fabrications of porous metal oxides. Inexpensive metal nitrate and glycine (the simplest amino acid) are used as raw

materials. The synthesis of cobalt-based amorphous precursor is similar to our previous report for synthesis of a zinc-based amorphous precursor, which, upon a subsequent calcination, decomposed to form macroporous ZnO networks.³⁷ For a convenient observation of the synthesis process of the cobalt-based complex, the solution was also heated on a hot plate maintained at 400 °C, and the photographs taken at different reaction stages are exhibited in Fig. S1 in the Electronic Supplementary Information (ESI[†]). Once being placed on the hot plate, the solution rapidly boiled (Fig. S1a). After several minutes, the initial pink color turned to blue (Fig. S1b), which is attributed to the change in the coordination environment of Co, namely, the gradual loss of its crystal water. The xerogel bubbled, decomposed and released lots of gases, resulting in the further change of color to black (Fig. S1c). Finally, a black product formed (Fig. S1d). The whole synthesis duration on the hot plate is shorter than that in furnace because of the difference in heat transfer conditions. The as-synthesized precursor was then calcined in air to obtain a porous metal oxide network.

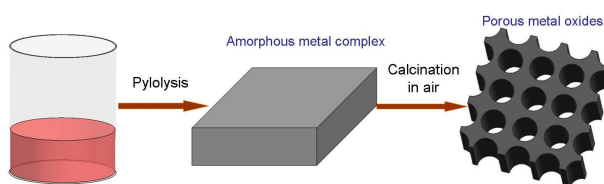


Fig. 1 A schematic illustration of the synthesis procedure for porous metal oxides.

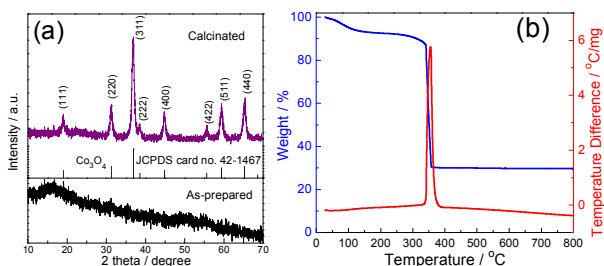


Fig. 2 (a) XRD patterns of the as-synthesized and calcinated powders, (b) TG-DTA curves of the as-synthesized powder.

No obvious diffraction peaks can be detected in the X-ray diffraction (XRD) pattern of the as-synthesized precursor (Fig. 2a), indicating its amorphous feature. The energy dispersive spectrum (EDS, Fig. S2) shows that the precursor contains Co, O, N, and C elements. The content of C, N, and H measured by an element analysis (Flash EA 1112, ThermoFinnigan) is 34.55 wt. %, 19.27 wt. % and 2.23 wt. %, respectively. X-ray photoelectron spectra (XPS) were carried out to further investigate the composition of the cobalt-based complex and the results are shown in Fig. S3. The Co 2p spectrum in Fig. S3a shows four peaks of the 2p_{3/2} and 2p_{1/2} doublet. The Co 2p_{3/2} and 2p_{1/2} binding energies at ca. 780.5 and 796.7 eV are in good agreement with the energies of the photoelectrons of Co²⁺.³⁸ The O 1s at 531.1 eV is attributed to O-Co bonds,³⁸ and the peak at 532.6 eV corresponds to covalent bonds of O with H or/and C.³⁹ The C 1s spectrum can be fitted into three peaks around 284.5, 285.5, and 287.4 eV, corresponding to the C-C, C-OH/C-N, and O=C-O

bonds, respectively.^{40,41} The N 1s spectrum can be fitted to three peaks at 398.5, 399.7, and 401.0 eV, which may be assigned to Co-N bonds, N-H bonds,⁴² and ammonium ions/chemically absorbed nitrogen species,^{43,44} respectively.

Thermogravimetric and differential thermal analysis (TG-DTA) were performed in air atmosphere at a heating rate of 5 °C min⁻¹ from room temperature to 800 °C and the results are shown in Fig. 2b. A sharp weight loss accompanied by a strong exothermic peak at 355 °C can be found, which indicates the decomposition of the as-synthesized amorphous complex to Co₃O₄. The weight loss is assigned to the removal of organic components (C, N, H, and partial O), which resulted in the formation of porous structure in the calcined products. The decomposition temperature here is much lower than that of the amorphous zinc-based complex previously reported³⁷ (355 °C vs. 550 °C), which is beneficial for the formation of the present mesoporous Co₃O₄ network with fine particle sizes.

Fig. 3a, b shows a typical scanning electron microscopy (SEM) and transmission electron microscopy (TEM) image of the as-combusted precursor. A compact structure with smooth surface can be discerned. No recognizable lattice spacing can be observed in the high-resolution transmission electron microscopy (HRTEM) image. Moreover, the selected area electron diffraction (SAED) pattern (Fig. 3d) reveals a full halo ring without any obvious diffraction spots, further confirming the amorphous nature. Elements of Co, O, C, and N distributed homogeneously throughout the precursor, as shown in the EDS mapping (Fig. S4), because of the molecular level mixing of the initial solution.

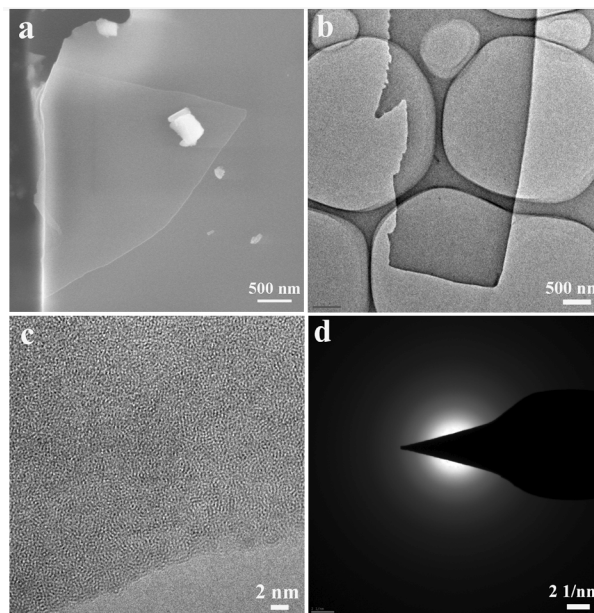


Fig. 3 SEM image (a), TEM image (b), HRTEM image (c), and selected area electron diffraction pattern (d) of the as-synthesized amorphous complex.

In calcination, cobalt components were oxidized to Co₃O₄ and the organic components were removed. As shown in Fig. 2a, all the diffraction peaks of the product can be indexed to the face-centered cubic spinel phase Co₃O₄ (JCPDS card No.

42-1467) after calcination at 355 °C for 1 h in air. The diffraction peaks at 19 °, 31.3 °, 36.9 °, 38.5 °, 44.8 °, 55.6 °, 59.4 °, and 65.2 ° are attributed to the (111), (220), (311), (222), (400), (422), (511), and (440) crystal plane, respectively. No other diffraction peaks can be observed, suggesting its high purity. The broad reflection peaks indicates small grains of Co₃O₄ and the grain size is determined to be ca. 12 nm by Scherrer formula. After the subsequent calcination in air, networks in micrometer-size with abundant pores are obtained (Fig. 4a, b). The irregular pores are mainly from several nanometers to tens of nanometers in size and the nanoparticles interconnect tightly with each other to construct a network. The particle size is also from several nanometers to tens of nanometers (Fig. 4b, c), which is consistent with the calculation result by Scherrer formula. In the HRTEM image (Fig. 4c), many atomic planes of spinal phase Co₃O₄, such as (111), (311), (400), and (220), are recognizable, demonstrating that the walls of porous Co₃O₄ is well crystallized. The SAED pattern (Fig. 4d) further confirms that the network is Co₃O₄ polycrystalline. The mass fraction of C and H in the sample is determined to be ca. 0.38% and 0.087%, respectively, and no N can be detected by element analysis. Trace N can be detected on the surface of the porous Co₃O₄ and the atomic ration of N/Co is determined to be ca. 0.03. The binding energy at ca. 400 eV (Fig. S5) may be attributed to adsorbed nitrogen species on the surface of porous Co₃O₄.⁴⁴ Further increasing the calcination temperature results in a higher crystallinity (Fig. S6) and larger particle size (Fig. S7), as well as larger pore size (Fig. S7), because of the enhanced grain growth. When calcinating at 550 °C, the product exhibits a worm-like porous structure (Fig. S7b), which is similar to porous metals prepared by a dealloying procedure.^{45,46}

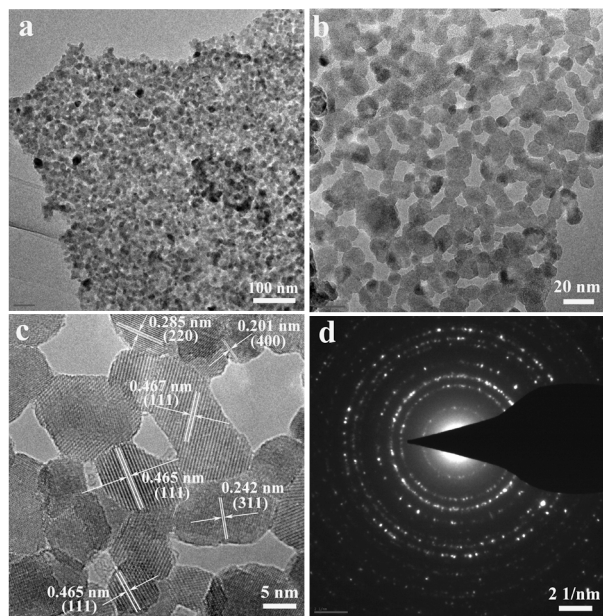


Fig. 4 TEM images (a, b), HRTEM image (c), and SAED pattern (d) of the porous Co₃O₄ network.

Nitrogen adsorption-desorption measurement was further performed to get more information about the porous structure.

The porous Co₃O₄ exhibited a type IV nitrogen isotherm (Fig. 5a), indicating the existence of mesopores. The specific surface area and total pore volume is determined to be 59 m² g⁻¹ and 0.261 cm³ g⁻¹, respectively. Fig. 5b shows the pore size distribution calculated by BJH method from the desorption branch. The pores range from several nanometers to tens of nanometers with a peak at ca. 15 nm, which is in accordance with TEM observations (Fig. 4b, c).

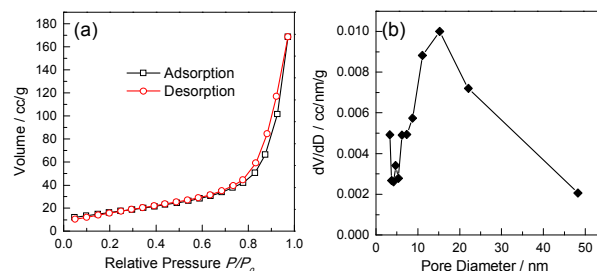
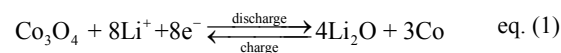


Fig. 5 (a) Nitrogen adsorption-desorption isotherm and (b) pore-size distribution of the porous Co₃O₄ network.

The lithium storage tests of the porous Co₃O₄ network as an anode material were performed in a potential window of 0.005–3.000 V versus Li. The electrochemical performance was evaluated in coin type lithium half-cells using Li foil as counter and reference electrodes at room temperature. The electrodes consisted of 80 wt. % Co₃O₄ powders, 10 wt. % acetylene black, and 10 wt. % polyvinylidene fluoride (PVDF). The active material (Co₃O₄) was 0.4–0.6 mg/cm² on each electrode and the coating thickness was ca. 3.5 μm. Fig. 6a illustrates the voltage profile. For the first discharge at a current density of 100 mA g⁻¹, the potential abruptly falls to about 1.14 V with a long plateau, which can be attributed to the reduction of Co₃O₄ to Co, followed by a sloping down to the cut-off voltage of 0.005 V, exhibiting a capacity of 1483 mAh g⁻¹. Fig. S8 shows the first two cyclic voltammetry (CV) curves at a scan rate of 0.1 mV s⁻¹ in a potential range of 0.005–3.0 V vs. Li/Li⁺. The peak at ca. 0.85 V in the first cathodic scan is attributed to the reduction of Co₃O₄ to Co accompanying the formation of Li₂O and the solid electrolyte interphase film.⁴⁷⁻⁴⁹ A peak at ca. 2.03 V in the first anodic process corresponds to the oxidation reaction from Co to Co₃O₄ accompanying the decomposition of Li₂O. In the second cycle, the cathodic peak shifts to a higher potential of ca. 1.04 V.⁴⁷⁻⁴⁹ The irreversible capacity in the first cycle is attributed to the formation of the SEI layer and some undecomposed Li₂O phase, which is common for metal oxide anodes. The initial coulombic efficiency of the porous Co₃O₄ is 71.1%. The reaction mechanism of Co₃O₄ with Li in lithium-ion batteries is proposed as follows⁵:



The porous Co₃O₄ exhibits a high discharge capacity of 1111 mAh g⁻¹ in the 2nd cycle at a high current of 100 mA g⁻¹. The discharge capacity of the present porous Co₃O₄ firstly decreases and then gradually increases during the discharge-charge cycling (Fig. 6b). After 100 cycles, the discharge capacity is 890 mAh g⁻¹, corresponding to 80% of the second

discharge capacity (Fig. 6b). At a much higher current density of 1000 mA g^{-1} , the second discharge capacity is still as high as 560 mAh g^{-1} and the capacity retains at 587 mAh g^{-1} after 500 cycles, exhibiting an extraordinary cycling stability (Fig. 5c). The parallel experiment indicates that the commercial Co_3O_4 nanoparticles show a rapidly decreased capacity, which is 403 mAh g^{-1} after 60 cycles at a current density of 100 mA g^{-1} (Fig. S9). The capacity increasing with cycling has been also seen in many cobalt oxides as well as other metal oxide anode materials.^{15,20,50-52} This phenomenon may be partly attributed to the reversible growth of a polymeric gel-like film resulting from the reaction of anode materials with electrolyte.⁵⁰

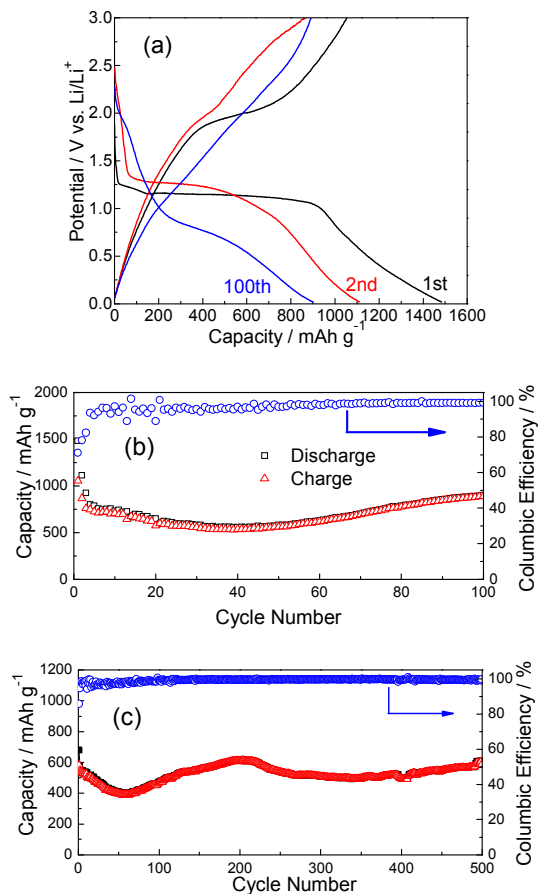


Fig. 6 Galvanostatic charge/discharge curves (a) and cycling performance of the porous Co_3O_4 network at a current density of 100 mA g^{-1} (b) and 1000 mA g^{-1} (c).

The porous Co_3O_4 delivers a discharge capacity of ca. 698, 600, 487, and 218 mAh g^{-1} at a current density of 500, 1000, 2000 and 5000 mA g^{-1} , respectively, as shown in Fig. S10. In the current investigation, the excellent electrochemical performance may be partly attributed to the low active material mass loading of $0.4\text{--}0.6 \text{ mg cm}^{-2}$, as superior electrochemical properties were frequently observed on low mass loading electrodes.^{53,54} By increasing the mass loading of active materials to $1.5\text{--}2.5 \text{ mg cm}^{-2}$, the discharge capacity of the porous Co_3O_4 decreases to ca. 964, 850, 690, and 505 mAh g^{-1} at a current density of 100, 200, 500 and 1000 mA g^{-1} , respectively (Fig. S11a). The cycling stability also

deteriorates (Fig. S11b). Recently, Sun et al reported a high-rate lithiation-induced reactivation of Co_3O_4 mesoporous hollow spheres due to the formation of a more open mesoporous structure and a thin and stable SEI.⁵² The reactivating process consists of three stages: I) capacity fading because of the mechanical degradation and unstable SEI; II) capacity reactivation; III) capacity stabilization.⁵² No capacity reactivation process can be observed for Co_3O_4 nanoparticles because pulverization instead of reactivation may occur, which may be attributed to a less open structure.⁵² In the current investigation, the poor cycling stability at a relatively high mass loading (Fig. S11) may be attributed to the high resistance and low reactivation efficiency. Because more active materials need longer cycles to fully reactivate electrodes and also the greater mass loadings result in slower transport.⁵²

The superior electrochemical performance of the porous Co_3O_4 could be attributed to the porous network structure. The porous architecture allows effective ion transportations and accommodates partially the large volume change during the cyclic process. According to eq. (1), the volume change of Co_3O_4 during lithium insertion/extraction processes is ca. 100%.⁵⁵ The large total pore volume ($0.261 \text{ cm}^3 \text{ g}^{-1}$) in the porous Co_3O_4 provides adequate space to accommodate the volume change. The porous structure is also advantageous to the reactivation process during cycling.⁵² The small particle size greatly decreases the diffusion time of lithium ions in Co_3O_4 , because diffusion time t is proportional to the square of the diffusion length L ($t \sim L^2 D^{-1}$). However, further work is needed to study the exact mechanism of the reactivation procedure and to improve the electrical conductivity of the porous Co_3O_4 , so as to improve the cycling stability at a high mass loading.

More importantly, the present synthesis strategy is universal and can be used to synthesize other metal oxides, such as porous ZnCo_2O_4 and porous NiO (the corresponding SEM images and XRD patterns are shown in Fig. S12 and S13, respectively).

In summary, porous Co_3O_4 networks were synthesized in a large scale by a simple top-down synthesis strategy. Firstly, an amorphous cobalt-based complex was prepared by a simple and rapid pyrolysis of a solution containing cobalt nitrate and glycine. Thermal decomposition of the cobalt-based complex in air results in the formation of the mesoporous Co_3O_4 network. The synthesis route is simple and the raw materials of metal nitrates and glycine are cheap and widely available. The mesoporous Co_3O_4 network exhibits a stable capacity of ca. 587 mAh g^{-1} for 500 cycles at a current density of 1000 mA g^{-1} at a low mass loading because of its porous structure as well as fine particle size. The porous architecture improves ion transportation and partially accommodates the large volume change during cyclic process. Furthermore, the small particle size greatly decreases the diffusion length of lithium ions. The present synthesis strategy can also be extended to mass productions of other porous metal oxides, such as porous ZnCo_2O_4 and porous NiO.

Acknowledgements

This work is supported by Zhejiang Provincial Natural Science Foundation of China under Grant No. LY13E020001. Dr. Wen thanks a scholarship award for Excellent Doctoral Student granted by Ministry of Education, China, for the financial support.

Notes and references

^a State Key Laboratory of Silicon Materials, Key Laboratory of Advanced Materials and Applications for Batteries of Zhejiang Province and Department of Materials Science and Engineering, Zhejiang University, Hangzhou 310027, P. R. China. Fax: +86 0571 87953115; E-mail: msewjim@zju.edu.cn

^b Key Laboratory of Cluster Science, Ministry of Education of China and Department of Chemistry, Beijing Institute of Technology, Beijing 100081, P. R. China.

[†] Electronic Supplementary Information (ESI) available: Experimental details and additional characterizations of photographs, EDS, XPS, XRD, and SEM images. See DOI: 10.1039/b000000x/

- M. Armand and J. M. Tarascon, *Nature*, 2008, **451**, 652.
- Z. Yang, J. Zhang, M. C. W. Kintner-Meyer, X. Lu, D. Choi, J. P. Lemmon and J. Liu, *Chem. Rev.*, 2011, **111**, 3577.
- B. Dunn, H. Kamath and J. M. Tarascon, *Science*, 2011, **334**, 928.
- N. Liu, Z. Lu, J. Zhao, M. T. McDowell, H. W. Lee, W. Zhao and Y. Cui, *Nat. Nanotechnol.* 2014, **9**, 187.
- P. Poizot, S. Laruelle, S. Grugeon, L. Dupont and J. M. Tarascon, *Nature*, 2000, **407**, 496.
- J. Cabana, L. Monconduit, D. Larcher and M. R. Palacin, *Adv. Mater.*, 2010, **22**, E170.
- W. Wen, J. M. Wu and J. P. Tu, *J. Alloys Compd.*, 2012, **513**, 592.
- J. Hu, Z. Wen, Q. Wang, X. Yao, Q. Zhang, J. Zhou and J. Li, *J. Phys. Chem. B* 2006, **110**, 24305.
- X. W. Lou, D. Deng, J. Y. Lee, J. Feng and L. A. Archer, *Adv. Mater.*, 2008, **20**, 258.
- K. T. Nam, D. W. Kim, P. J. Yoo, C. Y. Chiang, N. Meethong, P. T. Hammond, Y. M. Chiang and A. M. Belcher, *Science*, 2006, **312**, 885.
- J. Ryu, S. K. Kim, K. Kang and C. B. Park, *ACS Nano*, 2010, **4**, 159.
- L. Tian, H. Zou, J. Fu, X. Yang, Y. Wang, H. Guo, X. Fu, C. Liang, M. Wu, P. K. Shen and Q. Cao, *Adv. Funct. Mater.*, 2010, **20**, 617.
- Y. Fan, H. Shao, J. Wang, L. Liu, J. Zhang and C. Cao, *Chem. Comm.*, 2011, **47**, 3469.
- X. Wang, H. Guan, S. Chen, H. Li, T. Zhai, D. Tang, Y. Bando and D. Golberg, *Chem. Comm.*, 2011, **47**, 12280.
- L. Li, K. H. Seng, Z. Chen, Z. Guo and H. K. Liu, *Nanoscale*, 2013, **5**, 1922.
- D. Liu, X. Wang, X. Wang, W. Tian, Y. Bando and D. Golberg, *Sci. Rep.*, 2013, **3**, 2543.
- J. Wang, N. Yang, H. Tang, Z. Dong, Q. Jin, M. Yang, D. Kisailus, H. Zhao, Z. Tang and D. Wang, *Angew. Chem. Int. Ed.*, 2013, **52**, 6417.
- C. T. Hsieh, J. S. Lin, Y. F. Chen and H. Teng, *J. Phys. Chem. C*, 2012, **116**, 15251.
- B. Li, H. Cao, J. Shao, G. Li, M. Qu and G. Yin, *Inorg. Chem.*, 2011, **50**, 1628.
- Z. S. Wu, W. Ren, L. Wen, L. Gao, J. Zhao, Z. Chen, G. Zhou, F. Li and H. M. Cheng, *ACS Nano*, 2010, **4**, 3187.
- C. Peng, B. Chen, Y. Qin, S. Yang, C. Li, Y. Zuo, S. Liu and J. Yang, *ACS Nano*, 2012, **6**, 1074.
- X. L. Huang, R. Z. Wang, D. Xu, Z. L. Wang, H. G. Wang, J. J. Xu, Z. Wu, Q. C. Liu, Y. Zhang and X. B. Zhang, *Adv. Funct. Mater.*, 2013, **23**, 4345.
- Y. Yu, C. H. Chen, J. L. Shui and S. Xie, *Angew. Chem. Int. Ed.*, 2005, **44**, 7085.
- Y. Li, B. Tan and Y. Wu, *Nano Lett.*, 2008, **8**, 265.
- X. Y. Xue, S. Yuan, L. L. Xing, Z. H. Chen, B. He and Y. J. Chen, *Chem. Comm.*, 2011, **47**, 4718.
- D. H. Ha, M. A. Islam and R. D. Robinson, *Nano Lett.*, 2012, **12**, 5122.
- J. F. M. Oudenhoven, L. Baggetto and P. H. L. Notten, *Adv. Energy Mater.*, 2011, **1**, 10.
- A. Vu, Y. Qian and A. Stein, *Adv. Energy Mater.*, 2012, **2**, 1056.
- H. W. Shim, A. H. Lim, J. C. Kim, E. Jang, S. D. Seo, G. H. Lee, T. D. Kim and D. W. Kim, *Sci. Rep.*, 2013, **3**, 2325.
- C. Yuan, L. Yang, L. Hou, L. Shen, X. Zhang and X. W. Lou, *Energy Environ. Sci.*, 2012, **5**, 7883.
- S. Xiong, J. S. Chen, X. W. Lou and H. C. Zeng, *Adv. Funct. Mater.*, 2012, **22**, 861.
- X. Xu, R. Cao, S. Jeong and J. Cho, *Nano Lett.*, 2012, **12**, 4988.
- L. Zhang, H. B. Wu, S. Madhavi, H. H. Hng and X. W. Lou, *J. Am. Chem. Soc.*, 2012, **134**, 17388.
- F. Meng, Z. Fang, Z. Li, W. Xu, M. Wang, Y. Liu, J. Zhang, W. Wang, D. Zhao and X. Guo, *J. Mater. Chem. A*, 2013, **1**, 7235.
- L. Hu, Y. Huang, F. Zhang and Q. Chen, *Nanoscale*, 2013, **5**, 4186.
- L. Hu and Q. Chen, *Nanoscale*, 2014, **6**, 1236.
- W. Wen, J. M. Wu and Y. D. Wang, *Appl. Phys. Lett.*, 2012, **100**, 262111.
- Y. Sun, X. Hu, W. Luo and Y. Huang, *J. Mater. Chem.*, 2012, **22**, 13826.
- S. S. Shinde, P. S. Shinde, Y. W. Oh, D. Haranath, C. H. Bhosale and K. Y. Rajpure, *J. Anal. Appl. Pyrolysis*, 2012, **97**, 181.
- L. Lai, J. Zhu, Z. Li, D. Y. W. Yu, S. Jiang, X. Cai, Q. Yan, Y. M. Lam, Z. Shen and J. Lin, *Nano Energy*, 2014, **3**, 134.
- Z. H. Sheng, L. Shao, J. J. Chen, W. J. Bao, F. B. Wang and X. H. Xia, *ACS Nano*, 2011, **5**, 4350.
- P. Cao, D. X. Zhao, J. Y. Zhang, D. Z. Shen, Y. M. Lu, B. Yao, B. H. Li, Y. Bai and X. W. Fan, *Appl. Surf. Sci.*, 2008, **254**, 2900.
- P. Liu, H. Zhang, H. Liu, Y. Wang, X. Yao, G. Zhu, S. Zhang and H. Zhao, *J. Am. Chem. Soc.* 2011, **133**, 19032.
- R. Asahi, T. Morikawa, T. Ohwaki, K. Aoki and Y. Taga, *Science*, 2001, **293**, 269.
- J. Erlebacher, M. J. Aziz, A. Karma, N. Dimitrov and K. Sieradzki, *Nature*, 2001, **410**, 450.
- X. Lang, A. Hirata, T. Fujita and M. Chen, *Nat. Nanotechnol.*, 2011, **6**, 232.
- L. Hu, N. Yan, Q. Chen, P. Zhang, H. Zhong, X. Zheng, Y. Li and X. Hu, *Chem. Eur. J.*, 2012, **18**, 8971.
- G. Zhou, L. Li, Q. Zhang, N. Li and F. Li, *Phys. Chem. Chem. Phys.*, 2013, **15**, 5582.
- W. Yuan, J. Zhang, D. Xie, Z. Dong, Q. Su, G. Du, *Electrochimica Acta*, 2013, **108**, 506.
- X. Li, L. Qiao, D. Li, X. Wang, W. Xie and D. He, *J. Mater. Chem. A*, 2013, **1**, 6400.
- Y. Sun, X. Hu, W. Luo, F. Xia and Y. Huang, *Adv. Funct. Mater.*, 2013, **19**, 2436.
- H. Sun, G. Xin, T. Hu, M. Yu, D. Shao, X. Sun and J. Lian, *Nat. Commun.*, 2014, **5**, 4526.
- H. Wu, G. Chan, J. W. Choi, I. Ryu, Y. Yao, M. T. McDowell, S. W. Lee, A. Jackson, Y. Yang, L. Hu and Y. Cui, *Nat. Nanotechnol.*, 2012, **7**, 310.
- M. Wu, J. E. C. Sabisch, X. Song, A. M. Minor, V. S. Battaglia and G. Liu, *Nano Lett.*, 2013, **13**, 5397.
- K. H. Kim, D. W. Jung, V. H. Pham, J. S. Chung, B. S. Kong, J. K. Lee, K. Kim and E. S. Oh, *Electrochimica Acta*, 2012, **69**, 358.